Effect of Injection Routes on the Biodistribution, Clearance, and Tumor Uptake of Carbon Dots

Xinglu Huang,[†] Fan Zhang,[†,‡] Lei Zhu,[†,‡] Ki Young Choi,[†] Ning Guo,[†] Jinxia Guo,[†,‡] Kenneth Tackett,[§] Parambath Anilkumar,[§] Gang Liu,[‡] Qimeng Quan,[†] Hak Soo Choi,[⊥] Gang Niu,[†] Ya-Ping Sun,[§] Seulki Lee,[†] and Xiaoyuan Chen[†,*]

[†]Laboratory of Molecular Imaging and Nanomedicine (LOMIN), National Institute of Biomedical Imaging and Bioengineering (NIBIB), National Institutes of Health (NIH), Bethesda, Maryland 20892, United States, [‡]Center for Molecular Imaging and Translational Medicine, School of Public Health, Xiamen University, Xiamen 361005, China, [§]Department of Chemistry and Laboratory for Emerging Materials and Technology, Clemson University, Clemson, South Carolina 29634, United States, and [⊥]Division of Hematology/Oncology, Department of Medicine, Beth Israel Deaconess Medical Center, Boston, Massachusetts 02215, United States

ABSTRACT The emergence of photoluminescent carbon-based nanomaterials has shown exciting potential in the development of benign nanoprobes. However, the *in vivo* kinetic behaviors of these particles that are necessary for clinical translation are poorly understood to date. In this study, fluorescent carbon dots (C-dots) were synthesized and the effect of three injection routes on their fate *in vivo* was explored by using both near-infrared fluorescence and positron emission tomography imaging techniques. We found that C-dots are efficiently and rapidly excreted from the body after all three injection routes. The clearance rate of C-dots is ranked as intravenous > intramuscular > subcutaneous. The particles had relatively low retention in the reticuloendothelial system and showed high tumor-to-background contrast. Furthermore, different injection routes also resulted in different blood clearance patterns and tumor uptakes of C-dots. These results satisfy the need for clinical translation and should promote efforts to further investigate the possibility of using carbon-based nanoprobes in a clinical setting. More broadly, we provide a testing blueprint for *in vivo* behavior of nanoplatforms under various injection routes, an important step forward toward safety and efficacy analysis of nanoparticles.

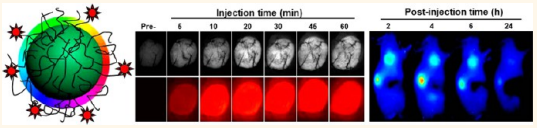

KEYWORDS: biodistribution · carbon dots · clearance · injection routes · translation · tumor uptake

Luminescent semiconductor quantum dots (QDs) have generated much excitement for a wide variety of promising applications in biolabeling and bioimaging fields.[1−8] However, the known toxicity and potential environmental hazard of these inorganic nanomaterials containing heavy metals such as cadmium limit their widespread use and *in vivo* applications in humans.[9−13] The emergence of photoluminescent carbon-based nanomaterials provides an exciting opportunity in the search for benign (nontoxic) alternative fluorescent nanomaterials and might offer great potential for optical imaging and related biomedical applications. These surface-functionalized carbon nanodots (C-dots) with ultrasmall sizes were found to be physicochemically and photochemically stable.[14] Combined with their well-defined, ultrafine dimensions and a variety of simple, fast, and cheap synthetic routes available,[15−23] C-dots provide an encouraging technological platform as an alternative to other carbon-based nanomaterials such as fullerenes, nanodiamonds, and carbon nanotubes and are expected to have wide applications in preclinical and potentially clinical studies.[24]

Recently, Liu's group reported that C-dots do not have noticeable signs of toxicity in treated animals,[25] demonstrating the feasibility for *in vivo* applications. The successful translation of nanoparticle-based biomaterials requires nanoparticles (NPs) not only with well-controlled *in vivo* behavior[26,27] but also possessing the lowest possible likelihood of toxicity. The U.S. Food and Drug Administration (FDA) has demanded that the agents injected into the human body, especially diagnostic agents, should be cleared completely in a reasonable period of time,[28] that such agents should not accumulate in the body, and that their exposure time should be minimized. To date, the key determinants of NP biodistribution and clearance focus on the properties of NPs,

* Address correspondence to Shawn.Chen@nih.gov.

Received for review September 5, 2012 and accepted June 3, 2013.

Published online June 03, 2013
10.1021/nn401911k

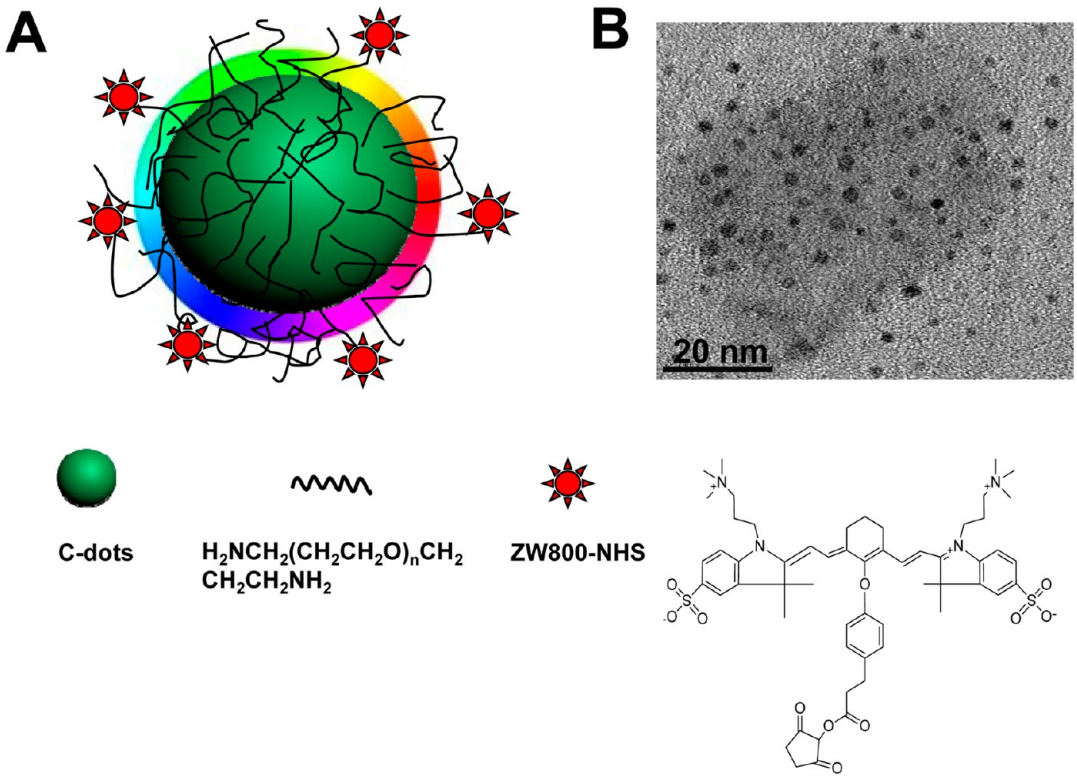

Figure 1. (A) Schematic structure of C-dot−ZW800 conjugate. (B) TEM image of C-dots.

such as the chemical composition, size, shape, and surface charge.[28−31] However, very few reports pay attention to factors applied in the clinic, such as injection or exposure routes, which are necessary for clinical translation of nanoformulations. Several studies reported significant differences in NP toxicity based on different exposure routes.[32,33] Although meaningful progress has been made in the synthesis strategy of C-dots, there is no report of C-dots that can target a disease state and can be efficiently cleared from the body after different injection routes.

RESULTS AND DISCUSSION

Fabrication and Characterization of near-Infrared C-Dots. Herein, we prepared near-infrared fluorescent C-dots (Figure 1A) by coupling the nanoparticles with the near-infrared dye ZW800, to track their *in vivo* fates and the effect of tumor uptake after three injection routes: intravenous (iv), subcutaneous (sc), and intramuscular (im), respectively. In a typical preparation, the C-dots were first synthesized according to a previously reported method.[21,22,34] Subsequently, surface passivation of C-dots was performed by reacting with diamine-terminated oligomeric poly(ethylene glycol). Three major purposes were implemented in the surface passivation process: (1) generation of bright luminescence;[21] (2) improvement of hydrophilicity and stability; (3) surface functionalization of C-dots. TEM imaging shows ultrasmall surface passivated C-dots of ~3 nm (Figure 1B).

The photoluminescence from C-dots is most likely attributed to the presence of surface energy traps that become emissive upon stabilization as a result of surface passivation.[21] Currently, a major reason limiting *in vivo* applications of C-dots is their low quantum yields in the near-infrared (NIR) region (650−900 nm), an ideal tissue fluorescence imaging window with low tissue absorption and scattering.[35−37] To improve the emission ability of C-dots in the NIR region, ZW800 (excitation ~770 nm, emission ~795 nm) was introduced onto C-dots by conjugating the dye NHS ester with amino groups on the C-dots, to make ZW800-labeled C-dots (C-dot−ZW800). There are about 20 dye molecules per particle on average, as estimated by quantifying the fluorescence intensity and absorbance values of ZW800 before and after conjugation. C-dot−ZW800 has absorption peaks at approximately 420 nm (C-dots) and 770 nm (ZW800) (Figure 2A) and two emission peaks at approximately 510 and 800 nm after excitation, respectively (Figure 2B). The imaging ability of C-dot−ZW800 in the visible and in the NIR range was also shown after excitation at different wavelengths by a Maestro all-optical imaging system (Figure 2C). Furthermore, the low fluorescence background of C-dot−ZW800 was shown in different biological fluids, such as fetal bovine serum (FBS), blood, urine, and tissue lysate (Supporting Information Figure S1). To better study the *in vivo* kinetics of C-dots, we also explored the fluorescence stability and particle stability of C-dot−ZW800. The fluorescence stability of C-dot−ZW800 was observed in

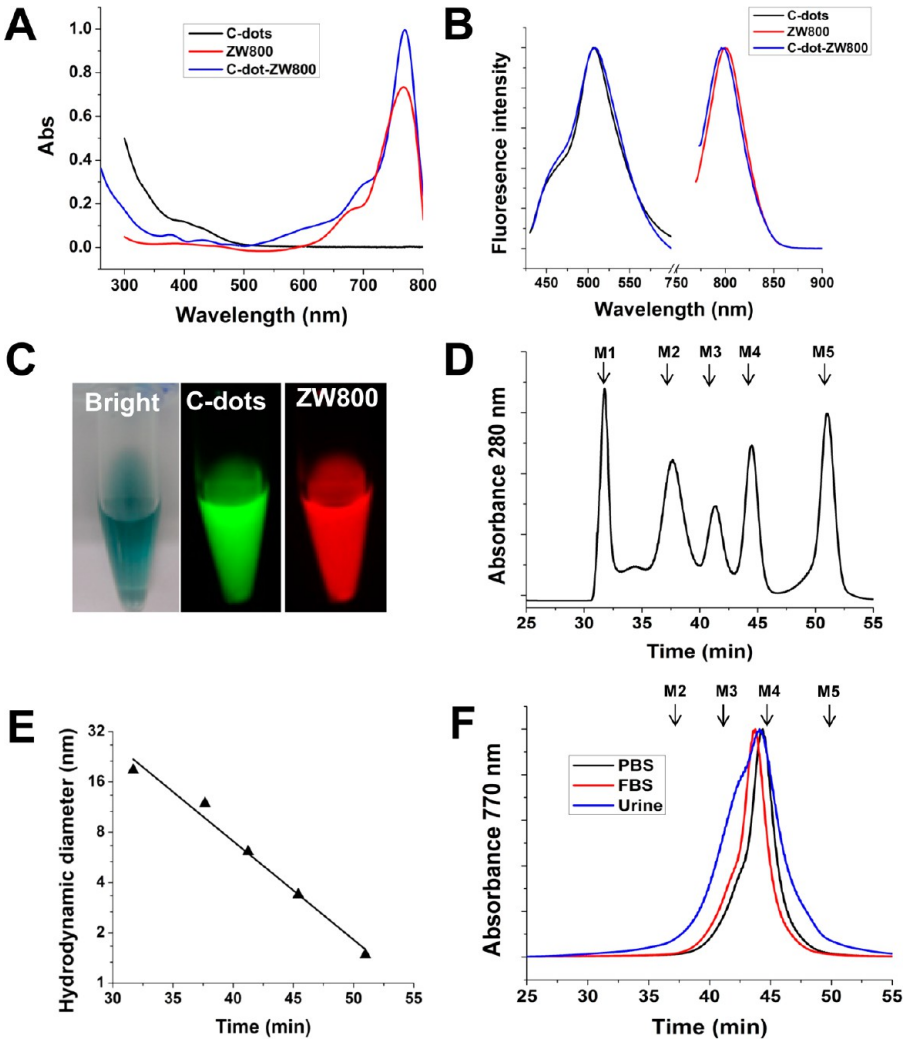

Figure 2. Optical properties and hydrodynamic diameters (HD) of C-dot−ZW800. Representative (A) absorbance and (B) fluorescence emission (λ_{Ex} = 420, 770 nm) spectra of C-dots, ZW800, and C-dot−ZW800. (C) Fluorescence images of C-dot−ZW800 based on C-dots and ZW800 by a Maestro imaging system, respectively. (D) Gel-filtration chromatography (GFC) analysis of protein standards (PBS, pH = 7.4). Molecular weight markers M1 (thyroglobulin; 669 kDa, 18.8 nm HD), M2 (γ-globulin; 158 kDa, 11.9 nm HD), M3 (ovalbumin; 44 kDa, 6.13 nm HD), M4 (myoglobin; 17 kDa, 3.83 nm HD), and M5 (vitamin B_{12}; 1.35 kDa, 1.48 nm HD) are shown by arrows. The retention time of protein standards at an absorbance of 280 nm was analyzed by reversed-phase HPLC. (E) GFC standard curve between HD and retention time. (F) Stability of C-dot−ZW800 in PBS, FBS, and urine after 1 h incubation at 37 °C prior to loading onto the GFC column. The retention time of particles at an absorbance of 770 nm was analyzed by reversed-phase HPLC.

the urine and blood. As shown in Supporting Information Figure S2, the fluorescence signals derived from C-dots and ZW800 were virtually unaltered over extended incubation time.

In our previous study, we demonstrated that the naked C-dots bear negative charges due to the existence of −OH/−COOH groups on the surface, with a zeta potential of −24 mV.[38] After passivation with PEG-amine, the zeta potential of C-dots was −14.3 ± 2.8 mV, and after further modification with ZW800 dye molecules,[39] the zeta potential of C-dot−ZW800 became −9.4 ± 4.6 mV. Dynamic light scattering (DLS) is a notoriously inaccurate technique for the characterization of weakly scattering colloids with small sizes, such as these C-dots, in contrast with highly scattering materials such as gold. To better define the hydrodynamic diameter (HD) of particles, a gel-filtration chromatography (GFC) system was used to characterize small-sized NPs with various coatings according to previous reports.[29,40] First, the protein standards were analyzed using GFC, including M1 (thyroglobulin; 669 kDa, 18.8 nm HD), M2 (γ-globulin; 158 kDa, 11.9 nm HD), M3 (ovalbumin; 44 kDa, 6.13 nm HD), M4 (myoglobin; 17 kDa, 3.83 nm HD), and M5 (vitamin B_{12}; 1.35 kDa, 1.48 nm HD) (Figure 2D). Subsequently, a standard curve of HD *vs* retention time was established, and the HD of C-dot−ZW800 was calculated to be 4.1 nm based on its GFC retention time (Figure 2E). To measure whether there is potential adsorption of serum proteins, C-dot−ZW800 were incubated in PBS, FBS, or mouse urine for 1 h at 37 °C before loading onto the GFC column. As shown in Figure 2F, slight changes in

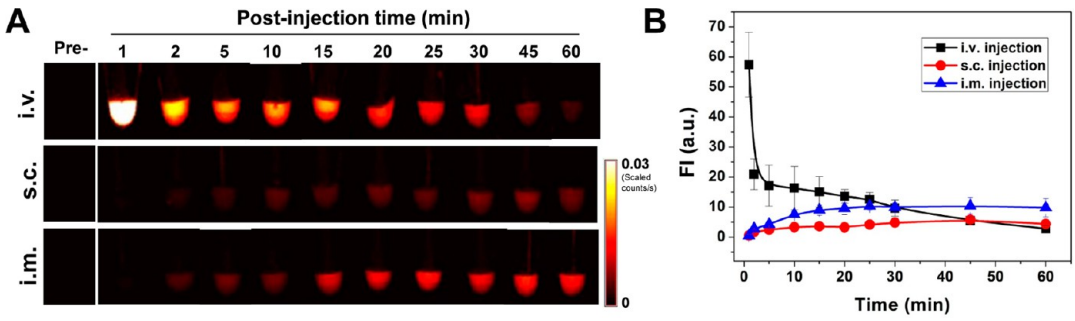

Figure 3. Blood circulation of C-dot−ZW800 after three injection routes. (A) After injection of particles, vein blood samples (5 μL) at indicated time points were collected into Eppendorf tubes containing 5 μL of heparin solution, and subsequently NIR fluorescence images were acquired. (Top) iv injection, (middle) sc injection, and (bottom) im injection. (B) Fluorescence time−activity curves derived from signals in (A).

the peak shape and retention time were found, indicating the possibility of adsorption of plasma protein onto the surface of C-dot particles.

Blood Circulation of Particles by Three Injection Routes. Before the NPs can be ready for clinical translation, a good understanding of their *in vivo* behavior is needed to minimize their potential toxicity. First, we studied the *in vivo* kinetics of C-dots by different injection routes. After injection of C-dots by three routes (iv, sc, and im), venous blood samples were collected at the indicated time points and subsequently analyzed by a Maestro all-optical imaging system. As shown in Figure 3, blood clearance rates of C-dot−ZW800 are rather different after different injection routes, according to the analysis of fluorescence signals from ZW800 dyes. The particle concentration in blood within 1 h dramatically decreased after iv injection (Figure 3A, top), while it was initially increased after sc (Figure 3A, middle) and im injection (Figure 3A, bottom) and then plateaued after 30 and 20 min postinjection, respectively. The quantitative analysis found that the particle fluorescence signal in blood at 1 min after iv injection was 17.3 ± 4.6-fold higher than 60 min (n = 4/group, Figure 3B). On the other hand, both sc and im injection groups showed lower particle concentration at 1 min postinjection than that at 60 min by 4.4 ± 1.3-fold and 9.6 ± 2.6-fold, respectively. To further confirm the particle concentration, representative fluorescence images of the collected blood at indicated time points after iv injection of C-dot−ZW800 were collected for C-dot and ZW800 (Supporting Information Figure S3). The same trend of blood clearance was observed for C-dots and ZW800, implying that the conjugated ZW800 dye molecules were not detached from the C-dot particles. We observed that the retention time of C-dot−ZW800 in blood after sc and im injection was significantly higher than that after iv injection, signifying the impact of injection route on the *in vivo* behaviors of given nanoparticles such as C-dots. It is speculated that the rapid blood clearance of C-dot−ZW800 might be due to serum protein adsorption onto the particle surface, leading to rapid opsonization followed by removal from the reticuloendothelial system.

Biodistribution of C-Dot Nanoparticles by Three Injection Routes. To minimize the toxicity of NPs, it is necessary to account for and completely remove all NPs from the body within a reasonable period of time. After being introduced into a living subject, NPs are typically metabolized *via* two major routes, the liver (into bile) and the kidneys (into urine).[41] To fully understand the clearance route of C-dots, organs were collected at 1 and 24 h after C-dot administration, and the biodistribution of particles was analyzed by quantitative *ex vivo* imaging. As shown in Figure 4A and Supporting Information Figure S4A, the majority of C-dot−ZW800 particles were accumulated in the kidneys at 1 h after injection *via* all three routes; only a small amount went to the liver. The signal of C-dot−ZW800 in the kidneys at the 1 h time point was quantified and ranked based on the injection routes as im > sc > iv (Supporting Information Figure S4B). After 24 h, no significant signal was detected in any organ, suggesting that the particles were all cleared out of the body regardless of the injection route (Supporting Information Figure S4C).

To further validate the biodistribution results obtained from optical imaging, we also employed positron emission tomography (PET) imaging to visualize and quantify the *in vivo* kinetics of the C-dots. The biodistibution of ^{64}Cu−C-dot measured by region of interest (ROI) analysis showed a very similar pattern to that obtained from optical imaging (Figure 4B). At 24 h postinjection of ^{64}Cu−C-dot, the mice were euthanized and major organs and tissues including blood, muscle, liver, kidneys, spleen, heart, and lung were harvested and measured by gamma counting, revealing less than 1% ID/g radioactivity in any organ measured in all three injection routes (Figure 4C), indicating low accumulation of C-dots in the reticuloendothelial system (RES) and rapid clearance from the body. On the basis of these results, it was concluded that C-dots were mainly excreted *via* the renal route into urine.

Urine Clearance of Particles by Three Injection Routes. Urine clearance analysis of C-dots after three injection routes was further performed in order to evaluate the *in vivo* behaviors of C-dots. The bladder of each mouse

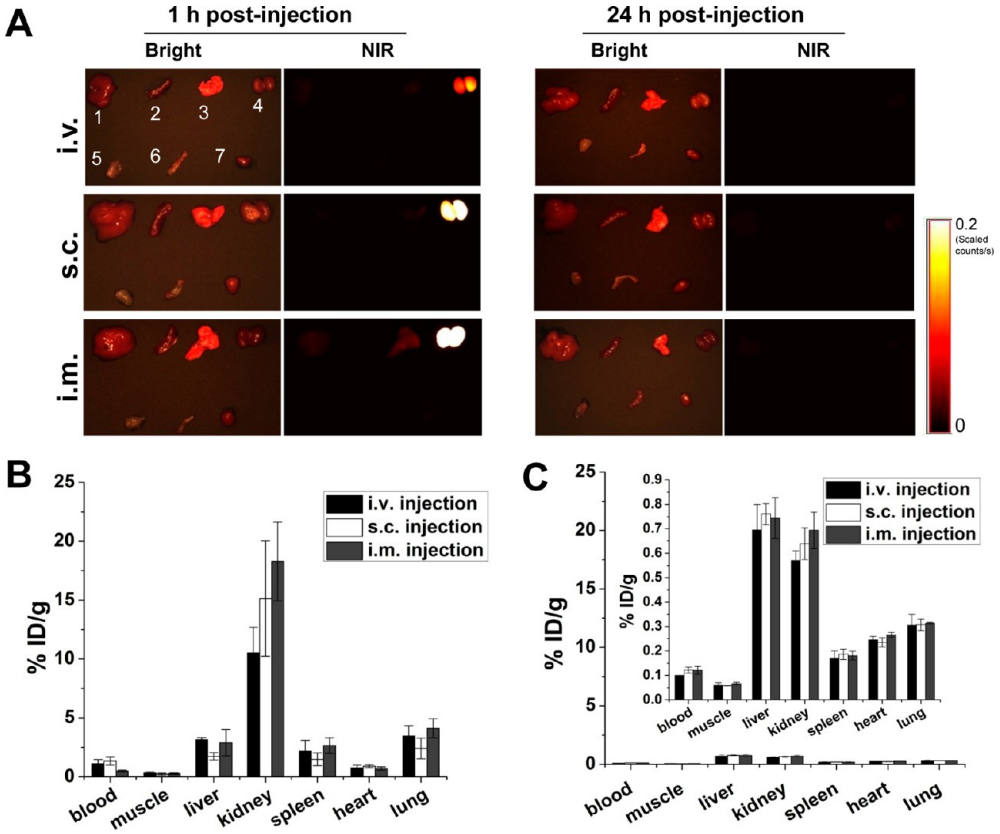

Figure 4. Biodistribution of particles after three injection routes. (A) *Ex vivo* **imaging of biodistribution of C-dot particles. After injection of particles, the major organs and tissues were harvested from Balb/C mice at the indicated time points, and subsequently, the bright field and NIR imaging were acquired using a Maestro imaging system. Left, 1 h postinjection (top, iv; middle, sc; bottom, im); right, 24 h postinjection (top, iv; middle, sc; bottom, im). Bright field: 1, liver; 2, spleen; 3, lung; 4, kidneys; 5, muscle; 6, intestine; 7, heart. (B, C) Quantification of the biodistribution of ^{64}Cu-labeled C-dots *via* three injection routes at 1 h (B) and 24 h (C) time points. At 1 and 24 h postinjection of ^{64}Cu−C-dot, the mice were euthanized and major organs and tissues including blood, muscle, liver, kidneys, spleen, heart, and lung were harvested and measured by gamma counting.**

after administration of C-dot−ZW800 was exposed and imaged at the indicated time points. The signal of C-dot−ZW800 was subsequently quantified to acquire a clearance curve. From Figure 5A and B, a rapid clearance is observed by iv injection, and the signal in the bladder plateaued 10 min after administration. Intravenous injection of C-dots displayed much faster urine clearance than the sc and im injection route within 10 min postinjection, respectively. To confirm the urine clearance of particles, bladder images were also acquired based on C-dot emission over time (Supporting Information S5). The urine displayed high background in the visible region, making it unsuitable for signal quantification. However, the signal from C-dot emission demonstrated the same trend of urine clearance as ZW800 emission, again indicating that the ZW800 fluorescence signal reflects C-dot−ZW800. The urine activity was also quantified by PET imaging (Figure 5C), which was in good accordance with the NIR fluorescence imaging results (Figure 5D). The amount of signals (both quantified from ZW800 fluorescence and ^{64}Cu radiolabel) in the urine within 1 h postinjection of ^{64}Cu−C-dot−ZW800 showed the pattern of iv > im > sc, in accordance with the clearance rate from the blood.

Accumulation of Particles at Injection Sites. Besides the accumulation in the RES, it is possible that the NPs accumulate at the injection site after sc and im administration (Figure 6A). For sc and im injection, most particles initially retained at the injection site have disappeared by 24 h postinjection. Quantitative analysis indicates that the signals at sc and im injection sites at the 24 h time point were 92.3 ± 10.2% and 99.1 ± 9.7% lower than those at 1 min postinjection, respectively (Figure 6B). These results elucidate that the NPs do not accumulate at the injection site and instead rapidly enter the blood circulation.

Tumor Uptake of Particles by Three Injection Routes. For cancer nanomedicine applications, it is desirable for NPs to have prominent and prolonged tumor uptake. C-dot−ZW800 particles were injected *via* three injection routes into athymic nude mice bearing subcutaneous SCC7 tumors. The images were acquired and analyzed on a Maestro all-optical imaging system. At 2 h postinjection, tumor was easily distinguishable from surrounding normal tissue in all three groups, and the tumor signal remained high over time (Figure 7A). In addition to the homogeneous uptake of C-dots in the solid tumors, most of the remaining C-dot−ZW800 were

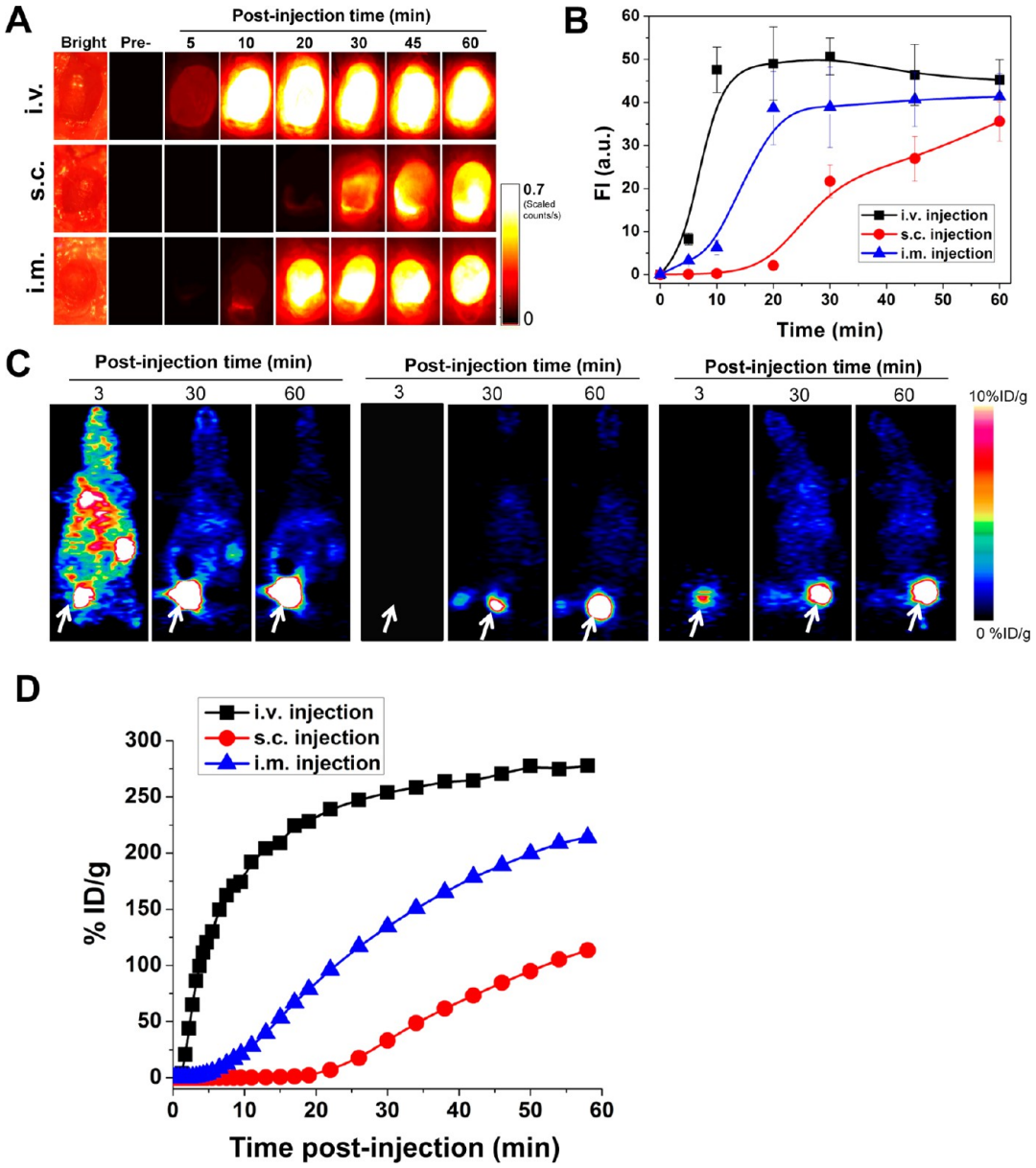

Figure 5. Urine accumulation of C-dot−ZW800 after different routes of injection. (A) The mice were kept under isoflurane anesthesia, the bladder was exposed, and NIR images were acquired at the indicated time points before and after (top) iv injection, (middle) sc injection, and (bottom) im injection. (B) Quantification of the ZW800 fluorescence signal in (A). (C) Representative coronal images from 1 h dynamic PET imaging of ^{64}Cu−C-dot after three routes of injection: left, iv injection; middle, sc injection; right, im injection. (D) Urinary bladder ROI analysis of the PET images in (C).

excreted through renal filtration (red arrow), as shown by high tumor-to-background ratio and low level of fluorescence in other tissues and organs. The iv group and sc group exhibited higher fluorescence signals in the tumor area than the im group at 2 h postinjection ($p < 0.05$) (Figure 7B). The sc group also showed somewhat stronger signal than the iv group in the tumor at 2, 4, and 24 h postinjection ($p > 0.05$), presumably due to the slower blood clearance of C-dots *via* sc than iv injection. The imaging results were further confirmed by *ex vivo* microscopic imaging of the frozen tissue slices obtained from mice sacrificed at 2 h postinjection (Figure 7C). Co-localization of C-dots and ZW800 in the tissue slices again excluded the possibility of dissociation of ZW800 from the C-dot−ZW800 conjugate.

In the present study, we found that C-dot−ZW800 particles were cleared mainly through the kidneys (into urine) and not the liver and spleen (Figure 4). NPs are often trapped in the RES (mainly liver and spleen) by macrophages, and PEGylation greatly reduces trapping by the RES compared with the naked NPs. It has been reported that for PEGylated QDs the hydrodynamic diameter has to be less than 5.5 nm for efficient renal excretion,[28−30,42] with clearance efficiency decreasing as hydrodynamic diameter increases. Our water-soluble C-dots with a core size of 3 nm and HD

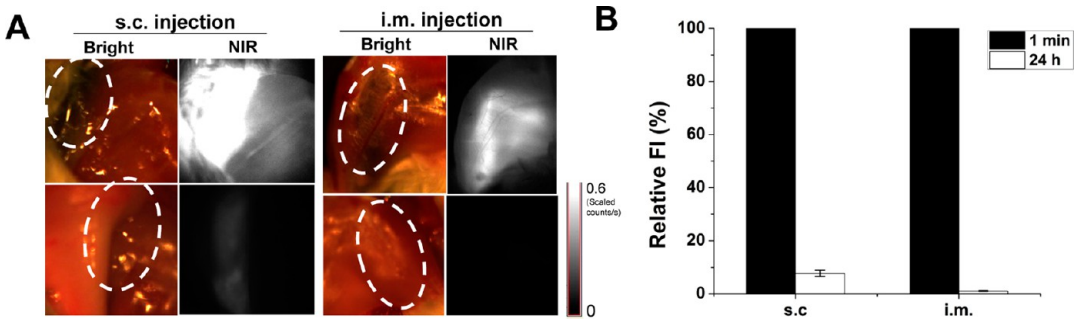

Figure 6. Accumulation of C-dot–ZW800 at sc and im injection sites. (A) NIR fluorescence images at (top) 1 min and (bottom) 24 h after sc injection and im injection: left, bright field images; right, NIR fluorescence images. The injection sites are indicated by circles. (B) Quantification of the relative fluorescence intensity at the injection sites over time.

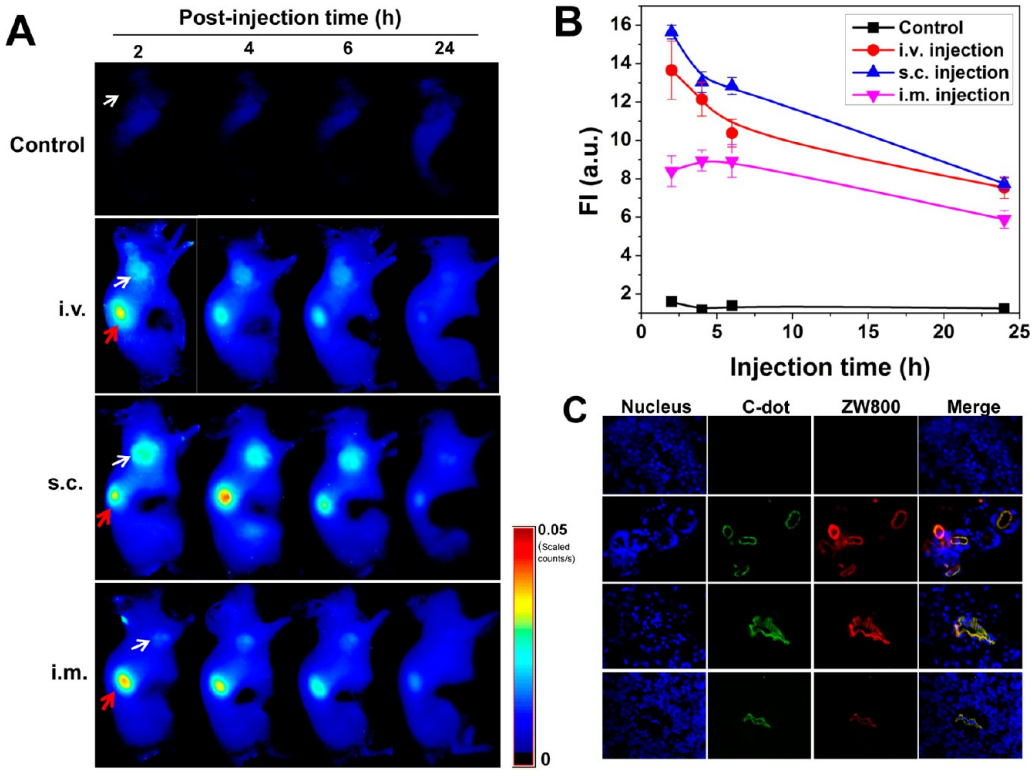

Figure 7. Tumor uptake of C-dot–ZW800 after different routes of injection. (A) NIR fluorescence images of SCC-7 tumor-bearing mice acquired at 2, 4, 6, and 24 h postinjection: control (without injection); iv injection; sc injection; im injection (white arrow indicates tumor; red arrow indicates kidney). (B) Tumor ROI analysis. Fluorescence signal unit: $\times 10^8$ photons/cm^2/s. (C) *Ex vivo* fluorescence images derived from the emission of C-dots and ZW800 were acquired to confirm tumor uptake of particles.

of 4.1 nm after PEGylation and ZW800 coupling led to rapid and efficient elimination of particles from the body *via* urinary excretion.

In clinical applications, different injection routes can be applied to fit special purposes, such as tumor targeting, long circulation, or ease of use by the physician. In this study, we illustrate that efficient clearance of C-dots is implemented not only after iv injection but also after sc and im injection with no significant accumulation at the injection sites over time (Figures 4 and 6). Owing to the presence of different biological barriers, the blood clearance and urine accumulation rate follow the order iv > im > sc (Figures 3 and 5). Furthermore, tumor uptake of C-dots by sc and iv injection was higher than that by im injection. This is probably due to the interplay among circulation time, clearance rate, and the concentration of particles retained in the tumor *via* different injection routes.[28] For example, we showed that the blood clearance of C-dots after iv injection was faster than the other two injection routes (Figure 5), which in turn could lead to reduced tumor retention. Thus, the *in vivo* behaviors of C-dots, such as the circulation time, major organ accumulation, and passive tumor targeting, can be easily controlled by the injection route. Overall, C-dots appear to have great potential as a

nanoplatform for preclinical biomedical research and translation into the clinic for optical imaging-guided surgery.

It is of note that while 2D fluorescence reflectance imaging used in this study is useful for qualitative and comparative analyses, it is unable to provide quantitative information, and it also does not allow for the assessment of C-dot accumulation in deeper-seated tissues. 3D fluorescence molecular tomography (FMT), based on volumetric reconstruction of the concentration of optical imaging agents, is generally considered to be able to overcome some of the shortcomings associated with 2D optical imaging and to enable more quantitative and more in-depth analyses.[43] Combining anatomical μCT with FMT may be applied in the future to noninvasively assess the biodistribution of C-dot–ZW800 conjugate in addition to radiolabeled C-dot–ZW800.

CONCLUSION

In summary, we explored the effects of different injection routes on blood circulation, biodistribution, urine clearance, and passive tumor uptake of C-dots. The C-dot–ZW800 conjugate was specifically designed to possess several significant features: NIR fluorescence emission, high stability *in vivo*, rapid renal clearance, and effective passive tumor targeting. Our studies suggest that the injection route affects the rate of blood and urine clearance, the biodistribution of C-dots in major organs and tissues, and tumor uptake over time. These characteristics make C-dot-based nanoprobes a viable candidate for clinical translation. We hope this study will lay the foundation for testing and designing targeted NPs with optimal exposure routes to control biodistribution, elimination from the body, and tumor targeting: key criteria for safety approval and clinical translation.

METHODS

Synthesis and Surface Passivation of C-Dots. Functionalized C-dots were synthesized according to previous reports.[21,34,44] Briefly, the C-dots were synthesized *via* laser ablation of a carbon target in the presence of water vapor with argon. Then, diamine-terminated oligomeric poly(ethylene glycol), $H_2NCH_2(CH_2CH_2O)_n$-$CH_2CH_2CH_2NH_2$ (n = 35, MW $\approx$ 1500, PEG_{1500N}), was used to react with the C-dots for surface passivation. In a typical reaction, PEG_{1500N} (200 mg, 0.13 mmol) was mixed with an acid-treated particle sample, and the mixture was heated to 120 °C for 72 h. After the reaction, the mixture was cooled to room temperature and dispersed in water, followed by centrifugation for 30 min. The supernatant containing C-dots was collected for further functionalization. The resulting particles were observed by transmission electron microscopy (TEM). The zeta potential of the particles was measured using a SZ-100 Nano Particle analyzer (Horiba Scientific).

Labeling of C-Dots with near-Infrared Dye ZW800 and PET Isotope ^{64}Cu. The near-infrared dye ZW800[35] was conjugated with C-dots by reaction between the amino groups of the C-dots and the NHS ester of ZW800. To remove free PEG before conjugation, the samples were purified by dialysis membrane (MW ~3500) in a PBS solution for 5 days by changing to fresh solution every 6–12 h. In a typical reaction, the C-dots (20 mg) were labeled with ZW800 (1 mg) in 10 mL of borate buffer (pH = 9.0) solution. The reaction mixture was stirred at room temperature for 4 h and then purified by a PD-10 desalting column (GE Healthcare). To make sure that free PEG–dye conjugate was completely removed, the product was further purified by dialysis membrane (MW ~3500) in a PBS solution for 3 days by changing to fresh solution every 6–12 h. Finally, the C-dot–ZW800 was concentrated into 5 mL of PBS and collected by a centrifugal filter (3k cutoff, Millipore). The UV–vis and fluorescence spectra of particles were recorded on a Genesys 10s UV–vis spectrophotometer (Thermo, IL, USA) and an F-7000 fluorescence spectrophotometer (Hitachi, Japan), respectively.

For ^{64}Cu labeling, the amino groups of C-dots were first conjugated with DOTA-NHS ester (Macrocyclics). Briefly, 5 mg of C-dots was reacted with 0.5 mg of DOTA-NHS ester in 2 mL of borate buffer (pH = 9.0). The mixture was stirred at room temperature for 4 h and subsequently purified by a PD-10 desalting column. The product was concentrated into 0.5 mL of PBS with a centrifugal filter. Then, the C-dot–DOTA conjugate was labeled with 1 mCi of ^{64}Cu for 1 h in NH_4Ac buffer (pH = 5.4) followed by PD-10 column purification. ^{64}Cu was produced at NIH by the irradiation of a thin layer of ^{64}Ni (Isoflex, USA) electroplated on a solid gold internal target plate of the CS-30 cyclotron utilizing the nuclear reaction ^{64}Ni(p,n)^{64}Cu and separated from the target material as $^{64}CuCl_2$ by anion chromatography.

Gel-Filtration Chromatography. Hydrodynamic diameters of particles were analyzed by GFC following a previous report.[5] Calibration of HD was performed by injecting 100 μL of protein standards (Bio-Rad, Hercules, CA, USA) containing thyroglobulin (M1, 669 kDa, 18.8 nm HD), γ-globulin (M2, 158 kDa, 11.9 nm HD), ovalbumin (M3, 44 kDa, 6.13 nm HD), myoglobin (M4, 17 kDa, 3.83 nm HD), and vitamin B_{12} (M5, 1.35 kDa, 1.48 nm HD). To measure whether serum proteins would be adsorbed onto C-dots, 1 mg/mL C-dot–ZW800 were incubated in PBS (pH = 7.4), 95% FBS, or 95% urine for 1 h at 37 °C before loading onto the GFC column.

Tissue Sample Collection and Analysis. Animal procedures were performed according to a protocol approved by the National Institutes of Health Clinical Center Animal Care and Use Committee (NIH CC/ACUC). After the injection of C-dot–ZW800, different organ and tissue samples were collected and analyzed. Briefly, C-dot–ZW800 in PBS solution (2.5 mg/kg, 50 μL) were injected by different routes (n = 4/group): intravenous injection (iv, tail vein), subcutaneous injection (sc, under the skin of left leg), and intramuscular injection (im, muscle of left leg), respectively. Blood samples (5 μL/withdrawal) were collected from the tail vein at different time points (1, 2, 5, 10, 15, 20, 25, 30, 45, and 60 min) postinjection of C-dot–ZW800. The samples were analyzed by a Maestro all-optical imaging system. For the urine clearance analysis, the mice were kept under isoflurane anesthesia (2% v/v isoflurane at 0.2 L min^{-1} O_2 flow), and the bladders of the mice were exposed. Subsequently, the bladders were imaged before and after three injection routes at indicated time points. Separate animals were also sacrificed, and different organs/tissues were collected at different time points for *ex vivo* fluorescence imaging. NIR fluorescence imaging was acquired by an appropriate filter set for ZW800 (excitation at 685–730 nm, emission at 745–800 nm) on a Maestro all-optical imaging system. The accumulation of particles at injection sites was also studied by exposing injection sites after different routes of injection and then imaged by a Maestro all-optical imaging system.

Tumor Inoculation and Imaging. The murine squamous cell carcinoma (SCC-7) cells were purchased from the American Type Culture Collection (ATCC, Rockville, MD, USA). The cells were maintained in RPMI 1640 medium (Invitrogen) supplemented with 10% FBS at 37 °C with 5% CO_2. Flank xenograft tumors were prepared by subcutaneous injection of 10^6 SCC-7 cells suspended in serum-free medium into each 5–7-week-old female athymic nude mouse. When the diameter of the tumors reached about 8 mm, the mice were divided into three groups (n = 4/group), and the C-dot–ZW800 particles (2.5 mg/kg, 50 μL) were injected by intravenous (iv), subcutaneous (sc), or intramuscular (im) route. The tumor uptake of particles was visualized and quantified by a Maestro all-optical imaging system.

Dynamic PET scans were performed using an Inveon micro-PET/CT scanner (Siemens Medical Solutions).[45] The dynamic PET data acquisition was started right before the injection (iv, sc, or im) of ^{64}Cu−C-dot (100 μCi/mouse, 50 μL). The body temperature of mice was maintained using a thermostat-controlled thermal heater. PET images were reconstructed by a two-dimensional ordered-subsets expectation maximum (OSEM) algorithm, and the frame rates were 10 × 30, 20 × 60, 5 × 120, and 5 × 300 s.

Histological Analysis. Tissue samples were snap-frozen, and 5 μm cryosections were prepared to check the biodistribution of particles by Olympus fluorescence microscopy. Specifically, the histology sections were washed twice with PBS and incubated with Z-fix solution for 10 min. Then, the histology sections were stained with 4′,6′-diamidino-2-phenylindole and observed under a fluorescence microscope. The signals derived from C-dots and ZW800 were observed by appropriate filters and software of the fluorescence microscope (Olympus IX81).

Statistical Analysis. The level of significance in all statistical analyses was set at a probability of $p < 0.05$. Data are presented as mean ± SD. Analysis of variance and *t* tests were used to analyze the data.

Conflict of Interest: The authors declare no competing financial interest.

Acknowledgment. This work was supported, in part, by the National Basic Research Program of China (973 Program 2013CB733802), the National Science Foundation of China (NSFC) (81201086, 81201129, 81101101, and 51273165), the Intramural Research Program of the NIBIB, NIH, and the Henry M. Jackson Foundation. S.L. was partially supported by an NIH Pathway to Independence (K99/R00) Award.

Supporting Information Available: Materials and methods section and additional figures. This material is available free of charge *via* the Internet at http://pubs.acs.org.

REFERENCES AND NOTES

1. So, M. K.; Xu, C.; Loening, A. M.; Gambhir, S. S.; Rao, J. Self-Illuminating Quantum Dot Conjugates for *in Vivo* Imaging. *Nat. Biotechnol.* **2006**, *24*, 339–343.
2. Gao, X.; Cui, Y.; Levenson, R. M.; Chung, L. W.; Nie, S. *In Vivo* Cancer Targeting and Imaging with Semiconductor Quantum Dots. *Nat. Biotechnol.* **2004**, *22*, 969–976.
3. Jaiswal, J. K.; Mattoussi, H.; Mauro, J. M.; Simon, S. M. Long-Term Multiple Color Imaging of Live Cells Using Quantum Dot Bioconjugates. *Nat. Biotechnol.* **2003**, *21*, 47–51.
4. Han, M.; Gao, X.; Su, J. Z.; Nie, S. Quantum-Dot-Tagged Microbeads for Multiplexed Optical Coding of Biomolecules. *Nat. Biotechnol.* **2001**, *19*, 631–635.
5. Cai, W.; Shin, D. W.; Chen, K.; Gheysens, O.; Cao, Q.; Wang, S. X.; Gambhir, S. S.; Chen, X. Peptide-Labeled near-Infrared Quantum Dots for Imaging Tumor Vasculature in Living Subjects. *Nano Lett.* **2006**, *6*, 669–676.
6. Gao, J.; Chen, K.; Xie, R.; Xie, J.; Lee, S.; Cheng, Z.; Peng, X.; Chen, X. Ultrasmall near-Infrared Non-Cadmium Quantum Dots for *in Vivo* Tumor Imaging. *Small* **2010**, *6*, 256–261.
7. Zhang, Y.; Wang, T. H. Quantum Dot Enabled Molecular Sensing and Diagnostics. *Theranostics* **2012**, *2*, 631–654.
8. Baba, K.; Nishida, K. Single-Molecule Tracking in Living Cells Using Single Quantum Dot Applications. *Theranostics* **2012**, *2*, 655–667.
9. Li, Y. F.; Chen, C. Fate and Toxicity of Metallic and Metal-Containing Nanoparticles for Biomedical Applications. *Small* **2011**, *7*, 2965–2980.
10. Ambrosone, A.; Mattera, L.; Marchesano, V.; Quarta, A.; Susha, A. S.; Tino, A.; Rogach, A. L.; Tortiglione, C. Mechanisms Underlying Toxicity Induced by CdTe Quantum Dots Determined in an Invertebrate Model Organism. *Biomaterials* **2012**, *33*, 1991–2000.
11. Chen, N.; He, Y.; Su, Y.; Li, X.; Huang, Q.; Wang, H.; Zhang, X.; Tai, R.; Fan, C. The Cytotoxicity of Cadmium-Based Quantum Dots. *Biomaterials* **2012**, *33*, 1238–1244.
12. Yang, Y.; Zhu, H.; Colvin, V. L.; Alvarez, P. J. Cellular and Transcriptional Response of Pseudomonas Stutzeri to Quantum Dots under Aerobic and Denitrifying Conditions. *Environ. Sci. Technol.* **2011**, *45*, 4988–4994.
13. Clift, M. J.; Stone, V. Quantum Dots: An Insight and Perspective of Their Biological Interaction and How This Relates to Their Relevance for Clinical Use. *Theranostics* **2012**, *2*, 668–680.
14. Baker, S. N.; Baker, G. A. Luminescent Carbon Nanodots: Emergent Nanolights. *Angew. Chem., Int. Ed.* **2010**, *49*, 6726–6744.
15. Fang, Y.; Guo, S.; Li, D.; Zhu, C.; Ren, W.; Dong, S.; Wang, E. Easy Synthesis and Imaging Applications of Cross-Linked Green Fluorescent Hollow Carbon Nanoparticles. *ACS Nano* **2012**, *6*, 400–409.
16. Lu, J.; Yang, J. X.; Wang, J.; Lim, A.; Wang, S.; Loh, K. P. One-Pot Synthesis of Fluorescent Carbon Nanoribbons, Nanoparticles, and Graphene by the Exfoliation of Graphite in Ionic Liquids. *ACS Nano* **2009**, *3*, 2367–2375.
17. Yang, Y.; Cui, J.; Zheng, M.; Hu, C.; Tan, S.; Xiao, Y.; Yang, Q.; Liu, Y. One-Step Synthesis of Amino-Functionalized Fluorescent Carbon Nanoparticles by Hydrothermal Carbonization of Chitosan. *Chem. Commun. (Cambridge, U.K.)* **2012**, *48*, 380–382.
18. Zhu, H.; Wang, X.; Li, Y.; Wang, Z.; Yang, F.; Yang, X. Microwave Synthesis of Fluorescent Carbon Nanoparticles with Electrochemiluminescence Properties. *Chem. Commun. (Cambridge, U.K.)* **2009**, 5118–5120.
19. Liu, H.; Ye, T.; Mao, C. Fluorescent Carbon Nanoparticles Derived from Candle Soot. *Angew. Chem., Int. Ed.* **2007**, *46*, 6473–6475.
20. Liu, R.; Wu, D.; Liu, S.; Koynov, K.; Knoll, W.; Li, Q. An Aqueous Route to Multicolor Photoluminescent Carbon Dots Using Silica Spheres as Carriers. *Angew. Chem., Int. Ed.* **2009**, *48*, 4598–4601.
21. Sun, Y. P.; Zhou, B.; Lin, Y.; Wang, W.; Fernando, K. A.; Pathak, P.; Meziani, M. J.; Harruff, B. A.; Wang, X.; Wang, H.; *et al.* Quantum-Sized Carbon Dots for Bright and Colorful Photoluminescence. *J. Am. Chem. Soc.* **2006**, *128*, 7756–7757.
22. Cao, L.; Wang, X.; Meziani, M. J.; Lu, F.; Wang, H.; Luo, P. G.; Lin, Y.; Harruff, B. A.; Veca, L. M.; Murray, D.; *et al.* Carbon Dots for Multiphoton Bioimaging. *J. Am. Chem. Soc.* **2007**, *129*, 11318–11319.
23. Peng, J.; Gao, W.; Gupta, B. K.; Liu, Z.; Romero-Aburto, R.; Ge, L.; Song, L.; Alemany, L. B.; Zhan, X.; Gao, G.; *et al.* Graphene Quantum Dots Derived from Carbon Fibers. *Nano Lett.* **2012**, *12*, 844–849.
24. Cao, L.; Yang, S. T.; Wang, X.; Luo, P. G.; Liu, J. H.; Sahu, S.; Liu, Y.; Sun, Y. P. Competitive Performance of Carbon "Quantum" Dots in Optical Bioimaging. *Theranostics* **2012**, *2*, 295–301.
25. Tao, H.; Yang, K.; Ma, Z.; Wan, J.; Zhang, Y.; Kang, Z.; Liu, Z. *In Vivo* NIR Fluorescence Imaging, Biodistribution, and Toxicology of Photoluminescent Carbon Dots Produced from Carbon Nanotubes and Graphite. *Small* **2011**, *8*, 281–290.
26. Gao, J.; Chen, K.; Luong, R.; Bouley, D. M.; Mao, H.; Qiao, T.; Gambhir, S. S.; Cheng, Z. A Novel Clinically Translatable Fluorescent Nanoparticle for Targeted Molecular Imaging of Tumors in Living Subjects. *Nano Lett.* **2012**, *12*, 281–286.
27. Choi, H. S.; Frangioni, J. V. Nanoparticles for Biomedical Imaging: Fundamentals of Clinical Translation. *Mol. Imaging* **2010**, *9*, 291–310.
28. Choi, H. S.; Liu, W.; Misra, P.; Tanaka, E.; Zimmer, J. P.; Itty Ipe, B.; Bawendi, M. G.; Frangioni, J. V. Renal Clearance of Quantum Dots. *Nat. Biotechnol.* **2007**, *25*, 1165–1170.
29. Choi, H. S.; Ipe, B. I.; Misra, P.; Lee, J. H.; Bawendi, M. G.; Frangioni, J. V. Tissue- and Organ-Selective Biodistribution of NIR Fluorescent Quantum Dots. *Nano Lett.* **2009**, *9*, 2354–2359.
30. Choi, H. S.; Liu, W.; Liu, F.; Nasr, K.; Misra, P.; Bawendi, M. G.; Frangioni, J. V. Design Considerations for Tumour-Targeted Nanoparticles. *Nat. Nanotechnol.* **2010**, *5*, 42–47.
31. Colvin, V. L. The Potential Environmental Impact of Engineered Nanomaterials. *Nat. Biotechnol.* **2003**, *21*, 1166–1170.
32. Sarlo, K.; Blackburn, K. L.; Clark, E. D.; Grothaus, J.; Chaney, J.; Neu, S.; Flood, J.; Abbott, D.; Bohne, C.; Casey, K.; *et al.* Tissue Distribution of 20 nm, 100 nm and 1000 nm

Fluorescent Polystyrene Latex Nanospheres Following Acute Systemic or Acute and Repeat Airway Exposure in the Rat. *Toxicology* **2009**, *263*, 117–126.
33. Zhang, X. D.; Wu, H. Y.; Wu, D.; Wang, Y. Y.; Chang, J. H.; Zhai, Z. B.; Meng, A. M.; Liu, P. X.; Zhang, L. A.; Fan, F. Y. Toxicologic Effects of Gold Nanoparticles *in Vivo* by Different Administration Routes. *Int. J. Nanomed.* **2010**, *5*, 771–781.
34. Yang, S. T.; Wang, X.; Wang, H.; Lu, F.; Luo, P. G.; Cao, L.; Meziani, M. J.; Liu, J. H.; Liu, Y.; Chen, M.; *et al*. Carbon Dots as Nontoxic and High-Performance Fluorescence Imaging Agents. *J. Phys. Chem. C Nanomater. Interfaces* **2009**, *113*, 18110–18114.
35. Filonov, G. S.; Piatkevich, K. D.; Ting, L. M.; Zhang, J.; Kim, K.; Verkhusha, V. V. Bright and Stable near-Infrared Fluorescent Protein for *in Vivo* Imaging. *Nat. Biotechnol.* **2011**, *29*, 757–761.
36. Welsher, K.; Sherlock, S. P.; Dai, H. Deep-Tissue Anatomical Imaging of Mice Using Carbon Nanotube Fluorophores in the Second near-Infrared Window. *Proc. Natl. Acad. Sci. U.S.A.* **2011**, *108*, 8943–8948.
37. Smith, A. M.; Mancini, M. C.; Nie, S. Bioimaging: Second Window for *in Vivo* Imaging. *Nat. Nanotechnol.* **2009**, *4*, 710–711.
38. Huang, P.; Lin, J.; Wang, X.; Wang, Z.; Zhang, C.; He, M.; Wang, K.; Chen, F.; Li, Z.; Shen, G.; *et al*. Light-Triggered Theranostics Based on Photosensitizer-Conjugated Carbon Dots for Simultaneous Enhanced-Fluorescence Imaging and Photodynamic Therapy. *Adv. Mater.* **2012**, *24*, 5104–5110.
39. Choi, H. S.; Nasr, K.; Alyabyev, S.; Feith, D.; Lee, J. H.; Kim, S. H.; Ashitate, Y.; Hyun, H.; Patonay, G.; Strekowski, L.; *et al*. Synthesis and *in Vivo* Fate of Zwitterionic Near-Infrared Fluorophores. *Angew. Chem., Int. Ed.* **2011**, *50*, 6258–6263.
40. Liu, W.; Choi, H. S.; Zimmer, J. P.; Tanaka, E.; Frangioni, J. V.; Bawendi, M. Compact Cysteine-Coated CdSe(ZnCdS) Quantum Dots for *in Vivo* Applications. *J. Am. Chem. Soc.* **2007**, *129*, 14530–14531.
41. Huang, X.; Li, L.; Liu, T.; Hao, N.; Liu, H.; Chen, D.; Tang, F. The Shape Effect of Mesoporous Silica Nanoparticles on Biodistribution, Clearance, and Biocompatibility *in Vivo*. *ACS Nano* **2011**, *5*, 5390–5399.
42. Praetner, M.; Rehberg, M.; Bihari, P.; Lerchenberger, M.; Uhl, B.; Holzer, M.; Eichhorn, M. E.; Furst, R.; Perisic, T.; Reichel, C. A.; *et al*. The Contribution of the Capillary Endothelium to Blood Clearance and Tissue Deposition of Anionic Quantum Dots *in Vivo*. *Biomaterials* **2010**, *31*, 6692–6700.
43. Kunjachan, S.; Gremse, F.; Theek, B.; Koczera, P.; Pola, R.; Pechar, M.; Etrych, T.; Ulbrich, K.; Storm, G.; Kiessling, F.; *et al*. Noninvasive Optical Imaging of Nanomedicine Biodistribution. *ACS Nano* **2013**, *7*, 252–262.
44. Yang, S. T.; Cao, L.; Luo, P. G.; Lu, F.; Wang, X.; Wang, H.; Meziani, M. J.; Liu, Y.; Qi, G.; Sun, Y. P. Carbon Dots for Optical Imaging *in Vivo*. *J. Am. Chem. Soc.* **2009**, *131*, 11308–11309.
45. Zhu, L.; Guo, N.; Li, Q.; Ma, Y.; Jacboson, O.; Lee, S.; Choi, H. S.; Mansfield, J. R.; Niu, G.; Chen, X. Dynamic PET and Optical Imaging and Compartment Modeling Using a Dual-Labeled Cyclic RGD Peptide Probe. *Theranostics* **2012**, *2*, 746–756.